Published in final edited form as:
Nat Neurosci. 2016 February ; 19(2): 299–307. doi:10.1038/nn.4197.

Thalamic nuclei convey diverse contextual information to layer 1 of visual cortex

Morgane M. Roth[#1], **Johannes C. Dahmen**[#2,3], **Dylan R. Muir**[#1], **Fabia Imhof**[1], **Francisco J. Martini**[1], and **Sonja B. Hofer**[1,2]

[1]Biozentrum, University of Basel, Switzerland [2]Department of Neuroscience, Physiology and Pharmacology, University College London, London, UK

[#] These authors contributed equally to this work.

Abstract

Sensory perception depends on the context within which a stimulus occurs. Prevailing models emphasize cortical feedback as the source of contextual modulation. However, higher-order thalamic nuclei, such as the pulvinar, interconnect with many cortical and subcortical areas, suggesting a role for the thalamus in providing sensory and behavioral context – yet the nature of the signals conveyed to cortex by higher-order thalamus remains poorly understood. Here we use axonal calcium imaging to measure information provided to visual cortex by the pulvinar equivalent in mice, the lateral posterior nucleus (LP), as well as the dorsolateral geniculate nucleus (dLGN). We found that dLGN conveys retinotopically precise visual signals, while LP provides distributed information from the visual scene. Both LP and dLGN projections carry locomotion signals. However, while dLGN inputs often respond to positive combinations of running and visual flow speed, LP signals discrepancies between self-generated and external visual motion. This higher-order thalamic nucleus therefore conveys diverse contextual signals that inform visual cortex about visual scene changes not predicted by the animal's own actions.

Introduction

Our perception of the environment relies on information flow from the sensory organs to the brain, where it is relayed through a cascade of increasingly sophisticated cortical processing stages. However, perception is also highly dependent on the context in which a given stimulus occurs, such as the sensory surround and the animal's behavioral state, its intentions, expectations and actions. Signals conveying contextual information are integrated with the feed-forward sensory signals already at the earliest stages of cortical processing.

Correspondence and request for materials should be addressed to SBH (sonja.hofer@unibas.ch).
[3]current address: Department of Physiology, Anatomy and Genetics, University of Oxford, Oxford, UK

Author contributions

JCD, MMR and SBH designed the experiments. JCD, MMR and FI performed the experiments and JCD, MMR and DRM analyzed the data. FJM performed electrophysiological recordings and analysis. SBH, JCD, MMR and DRM wrote the paper.

The authors declare no competing financial interests.

Europe PMC Funders Author Manuscripts

For instance, responses to visual stimuli in primary visual cortex (V1) can be modulated by the surrounding visual scene1, by the behavioral relevance of the stimulus2,3, or by the animal's locomotion4–6. While contextual signals are typically attributed to 'top-down' projections from other cortical areas3,7–10 or even neuromodulation11,12, accumulating evidence suggests that activity in sensory thalamic nuclei can also be modulated by behavioral state13–15. To understand how the thalamus contributes to contextual modulation of cortical sensory processing, it is important to determine what specific contextual signals are broadcast by the thalamus to primary sensory cortices. At present, the identity of these signals remains largely unknown.

There are two main nuclei in the thalamus engaged in visual processing16. The dorsal lateral geniculate nucleus (dLGN) is a first-order thalamic nucleus that is driven primarily by the retina, and projects to V1. In contrast, the pulvinar, the largest thalamic complex in humans, is a higher-order thalamic structure because it receives input from – and provides input to – most visual cortical areas16–21. The pulvinar exhibits complex visual response properties19,22, suggesting it constitutes a second major visual pathway that parallels direct cortico-cortical projections16. Indeed, the pulvinar can exert a strong influence on visual cortical areas23, including V124, and thus impacts visual processing at the earliest cortical stage. The pulvinar also receives input from many association, motor and visuo-motor areas, including prefrontal, parietal and cingulate cortex as well as the superior colliculus18,25–28. Consistent with its anatomy, the pulvinar has been implicated in a range of functions including visual attention, feature binding and spatial perception19. Moreover, pulvinar neurons respond to saccadic eye-movements and to intended motor actions such as arm reaching18,26.

By combining diverse information from multiple sources, the pulvinar has the potential to link sensory signals to visual and behavioral context. It could thus act as an internal reference that allows interpreting visual information in the context of the visual scene or an individual's motor actions. In such a scheme, visual and motor information may be integrated, for example, to encode signals that distinguish self-generated visual motion (caused by eye-movements or locomotion) from that of external objects. However, the properties of visual and non-visual signals the pulvinar conveys to V1 have not been characterized. Specifically, it is not known how V1-projecting pulvinar neurons integrate visual and motor information, and whether the nature of this visuomotor integration is different than in the dLGN, where activity is also modulated by locomotion in mice14.

To determine whether the pulvinar is part of a circuit that provides V1 with signals for contextual processing in general, and for visuomotor integration in particular, we characterized its homologue in rodents – the lateral posterior thalamic nucleus (LP). We reveal the anatomy of mouse LP, and determine visual and behavioral signals carried by LP projections into layer 1 (L1) of V1. We compare these signals to those of dLGN projections to the same layer, which might represent a pathway that is distinct from the main dLGN input in L429–31. We find that LP and dLGN projections are functionally distinct in several fundamental ways. Even in L1, dLGN projections are retinotopically highly ordered and convey spatially precise visual signals. In contrast, LP inputs provide distributed information from an expansive area of the visual scene. Both LP and dLGN projections additionally

carry motor signals related to saccades and locomotion. However, visuo-motor signals that differentiate between self-generated and external visual motion are predominantly transmitted by LP. This higher-order thalamic nucleus therefore conveys diverse contextual information to the cortex, including purely visual, purely motor, and visuo-motor interaction signals that concurrently inform V1 neurons of the broader visual scene and the animal's own actions.

Results

Afferent and efferent connectivity of mouse LP

To identify brain regions and neurons projecting to LP, we injected a retrograde tracer (cholera toxin subunit B; CTB) into this thalamic nucleus (Fig. 1a). LP received input from projection neurons in L5 and L6 of higher cortical visual areas, and from L5 and deep L6 neurons in primary visual cortex (V1; Fig. 1a). Substantial numbers of retrogradely labelled neurons were also found in cortical association areas, anterior cingulate cortex and superior colliculus (Fig. 1a, Supplementary Fig. 1). In turn, axons from LP targeted predominantly cortical areas from which it also received input, including all visual areas, but axonal projections were also visible in other other telencephalic structures (co-injection of AAV-GFP into LP; Supplementary Fig. 1). The reciprocal patterns of connectivity between LP and multiple cortical areas suggest that this thalamic nucleus is a central component of the visual processing hierarchy in the mouse32, similar to the pulvinar complex in higher mammals17,20,21.

In order to explore the topographic organization of thalamic input to visual cortex we injected three differently colored retrograde tracers at different retinotopic positions in V1 (Fig. 1b, Supplementary Fig. 2). As expected, retrogradely labelled neurons of different colors, projecting to different positions in V1, were clearly separated in dLGN consistent with their retinotopic map locations33. Retrogradely labelled neurons in LP formed partly overlapping clusters with some topographic organization and only few double-labelled cells (double-labelled cells: 3.2%, triple-labelled cells: 0.1%, 1952 cells, 3 mice). This suggests that LP neurons projecting to retinotopically different positions in V1 are coarsely spatially organized. In V1, LP axons projected to deeper layers as well as to L1 where they intermingled with axons from dLGN (Fig. 1c, AAV-tdTomato injected into LP, AAV-GFP injected into dLGN). LP and dLGN projections within layer 1 of V1 were spatially offset; dLGN axons were densest in deeper layer 1 whereas LP axons terminated more superficially (Fig. 1c; median ± interquartile range, dLGN: 53.8 ± 9.7 μm, LP: 37.5 ± 8.9 μm; $P = 0.03$, Wilcoxon rank-sum test).

Visual response properties of thalamic inputs into V1

What information do these two distinct thalamo-cortical pathways convey to V1? To address this question we used in vivo two-photon calcium imaging to functionally characterize visual input from dLGN and LP into V1. We used AAV vectors to express genetically encoded calcium indicator GCaMP5 or GCaMP634 either in LP or dLGN (Supplementary Fig. 3), and constructed a chronic imaging window over V1 (see Methods). We first recorded calcium transients in individual thalamo-cortical axons and putative axonal boutons35,36 in

layer 1 of V1 of lightly anaesthetized mice during presentation of gratings drifting in 12 different directions (Fig. 2). While a small subset of both LP and dLGN boutons showed selective responses to the grating stimuli, the majority responded to most grating directions. Consequently, the orientation selectivity index (OSI) for both LP and dLGN bouton populations was low, and slightly lower for LP than dLGN (Fig. 2a,b,d, median OSI, LP: 0.38 ± 0.23, dLGN: 0.44 ± 0.28; P = 0.012, Wilcoxon rank-sum test, Bonferroni-corrected for multiple comparisons here and for all comparisons below). In contrast, layer 2/3 neurons in V1 (AAV-GCaMP6 injection into V1) were much more orientation selective (Fig. 2c, median OSI: 0.74 ± 0.27; $P < 10^{-10}$, Wilcoxon rank-sum test). Similarly, the average direction selectivity (DSI) of both LP and dLGN boutons was substantially lower than that of neurons in V1 (Fig. 2e, median DSI, dLGN: 0.25 ± 0.26, LP: 0.27 ± 0.25, P = 0.12; V1: 0.51 ± 0.42, all P-values $< 10^{-8}$, Wilcoxon rank-sum test).

The similarity in orientation and direction selectivity of LP and dLGN boutons was unexpected given that the two thalamic nuclei receive different combinations of afferent inputs. We therefore characterized their visual response properties in more detail by mapping their spatial receptive field structure with sparse noise stimuli, and separately computed ON and OFF receptive field subdomains (Fig. 3a,b, Supplementary Fig. 4, see Methods). The receptive fields of the two thalamic projections showed pronounced differences. Receptive fields of LP boutons were much larger than those of dLGN boutons (Fig. 3c, median subfield area, LP: 415 ± 258 deg^2, dLGN: 183 ± 88 deg^2; $P < 10^{-10}$, Wilcoxon rank-sum test) or layer 2/3 neurons in V1 (median area: 246 ± 157 deg^2; all P-values $< 10^{-10}$, Wilcoxon rank-sum test). LP and dLGN receptive fields also differed in shape. The ON and OFF subfields of LP receptive fields were more elongated than dLGN and V1 subfields (Fig. 3d, Supplementary Fig 4, median aspect ratio of major over minor axis length, LP: 1.59 ± 0.58, dLGN: 1.26 ± 0.26, $P < 10^{-10}$; V1: 1.30 ± 0.34, V1-LP $P < 10^{-10}$, V1-dLGN P < 0.001, Wilcoxon rank-sum test). In addition, several other receptive field measures showed significant differences between dLGN and LP projections (Supplementary Fig. 4).

Similar results were obtained with electrophysiological single-unit recordings in the visual thalamus (Supplementary Fig. 5; see Methods). In addition, visually-evoked response latencies of LP neurons were about twice as long as those of dLGN neurons (Supplementary Fig. 5; mean latency ± s.e.m, LP: 187.5 ± 6.3 ms, dLGN: 93.8 ± 5.0 ms; $P < 10^{-6}$, Wilcoxon rank-sum test). Taken together, these results reveal fundamentally different visual response properties of LP and dLGN inputs in layer 1 of primary visual cortex. LP receptive fields are more heterogeneous, dispersed and much larger than those of both dLGN and V1, and their visual responses are delayed, consistent with LP receiving diverse inputs from various visual cortical areas16,17,19–21 (Fig. 1a).

Functional organization of thalamic inputs

A single field of view (120 x 120 μm^2) in layer 1 of V1 contained populations of up to a few hundred visually responsive thalamic boutons (Fig. 4a,b, Supplementary Figs. 3,6) carrying signals from several dozen different thalamic neurons (Supplementary Fig. 6). Receptive fields from populations of dLGN boutons within each 120 x 120 μm^2 region clustered in the

same part of the visual field (Fig. 4a), and the scatter of their receptive field centers was only slightly larger than that of layer 2/3 neurons within a V1 area of the same size (Fig. 4c,d, median pairwise distance between receptive field centers, dLGN: 9.30 ± 7.76 deg, V1: 7.42 ± 8.11 deg; all P-values < 10^{-10}, Wilcoxon rank-sum test). The degree of spatial precision of dLGN inputs into L1 was sufficient to observe fine-scale retinotopic organization of dLGN bouton receptive fields on a very local scale, even within individual imaged regions (Supplementary Fig. 7).

In contrast, receptive fields of populations of LP boutons were distributed over a much larger area of the visual field (Fig. 4b,d, median pairwise distance: 16.89 ± 16.27 deg; P < 10^{-10}, Wilcoxon rank-sum test), and little fine-scale retinotopic organization was apparent (Supplementary Fig. 7). Given the large scatter and size of LP receptive fields, the area of visual field covered by LP inputs to a given region of V1 was substantial (Fig. 4b,e). For dLGN bouton populations the visual field coverage increased as a function of the number of receptive fields sampled, but plateaued after a few dozen receptive fields for each dLGN bouton population with little jitter (Fig. 4e, median covered area, 1505 ± 380 deg^2, imaged regions with at least 50 receptive fields, n = 11). For LP bouton populations the visual field coverage was much larger and more variable for different imaged regions (median covered area: 3778 ± 1337 deg^2, n = 11; P < 0.001, Wilcoxon rank-sum test), and reached up to 5500 deg^2 – nearly three quarters of the visual field probed in our experiments (96 deg x 80 deg). Thus, LP input provides distributed information from an expansive area of the visual field to each local region in V1.

Taken together, layer 1 in primary visual cortex receives spatially precise visual input from the dLGN which covers a narrow area of the visual field, carried by boutons with small receptive fields that are retinotopically organized. In contrast, input from LP covers a large area of visual field carried by boutons with large receptive fields which do not show clear retinotopic organization on a local scale.

Motor signals in thalamo-cortical projections

In addition to visual areas, both LP and dLGN receive input from motor-related areas18,25,26,28, and motor-related signals have been observed in both the dLGN and the pulvinar of higher mammals14,18,26. Therefore either thalamic nucleus may be part of a sensory-motor integration circuit that interprets visual information in the context of motion generated by an animal’s own eye, head or body movements. To identify motor and visuo-motor signals in thalamic projections we imaged calcium responses of LP and dLGN boutons in V1 in awake, head-fixed mice running on a cylinder (Fig. 5a).

We first determined whether thalamic boutons carried signals related to saccade-like eye movements (Fig 5b,c). A small proportion of both LP and dLGN boutons was significantly modulated by saccades (Fig 5b,c). To test whether this signal was visually evoked or motor-related, we also tracked saccades in darkness (Supplementary Fig. 8). While LP showed a trend for fewer eye-movement modulated boutons, the fraction of dLGN boutons with saccade-related activity was significantly reduced in the dark (Fig. 5c; mean proportions light vs dark, dLGN: 6.2 ± 1.4 vs 2.6 ± 0.6, P = 0.03; LP: 9.8 ± 1.5 vs 6.2 ± 1.1; P = 0.06;

Wilcoxon rank-sum test). These results indicate that there are motor-related, saccadic signals in LP, consistent with data from the primate pulvinar26.

In order to understand how sensory and motor signals are represented in visual thalamic projections, and how these signals interact, it is important to separate the effects of these two variables on neuronal activity. Eye movements are not the only actions that lead to displacement of the visual scene on the retina. Another very salient sensory feedback signal is visual flow caused by whole body movements, for instance during locomotion. In our experiments, when animals were trained to run on the cylinder, their running controlled their position in a corridor with patterned walls in a virtual environment. The coupling of running speed to the virtual visual flow enabled active engagement with the visual environment. In some recordings, we then uncoupled the virtual visual flow ('visual flow' or VF) from locomotion by replaying corridor movies of previous sessions to the animals, irrespective of their running speed5,6 ('open-loop' condition). This allowed us to separately assess the effects of running speed and of the visual motion on the retina caused by visual flow that is under normal conditions associated with the animal's locomotion.

In the open-loop condition, subsets of LP and dLGN boutons responded not only to the visual flow of the virtual environment but also to locomotion (Fig. 6a,b), as was previously shown for dLGN14. Different boutons preferred specific speeds of visual flow or running, including those that increased or decreased their activity with increasing speed, as well as those with more complex, non-linear activity-speed relationships (Fig. 6a,b, Supplementary Fig. 9a,b). Comparable running-related activity was also apparent in the dark in both LP and dLGN boutons (Supplementary Fig. 9c,d). To capture both linear as well as non-linear relationships, we used a non-linear regression method to estimate the amount of information carried by individual boutons about running or visual flow speed in the open-loop condition. We trained a random forests decoding algorithm to predict these variables from the activity of each bouton36,37, whereby instantaneous speed (t) was predicted from short epochs of firing rate inferred from calcium signals centered on t (t ± 250 ms, see Methods).

The activity of some boutons was highly informative about running speed or visual flow speed, and therefore could be used to predict those variables well (Fig. 6c; PP: prediction power; correlation coefficient between predicted and observed speed traces). The proportions of these boutons were not different between dLGN and LP projections (Fig. 6c; for PP > 0.16; RS mean proportions, dLGN: 14 ± 3%, LP: 11 ± 1.9%, P = 0.27; VF mean proportions, dLGN: 11 ± 1.8% LP: 11 ± 0.9%, P = 0.94; Wilcoxon rank-sum test). Therefore, excitatory projections from both thalamic nuclei carry specific information about the animal's motor output as well as the visual flow normally experienced during self-motion.

Visuo-motor mismatch signals are enriched in LP boutons

Next, we examined how visual flow and running signals are integrated at the level of individual boutons. We plotted a signed PP – the sign indicates the preference of a bouton for high (positive) or low (negative) speeds – for visual flow speed against a signed PP for running speed for all boutons (Fig. 6d, see Methods). For those boutons highly informative about visual flow and/or running speed (PP > 0.16), we then computed an interaction angle

θ, which indicates the relative signed prediction power for those two variables (Fig. 6d,e, Supplementary Fig. 10; see Methods). Values of θ close to 0° or 180º indicate that a bouton selectively carries visual flow speed information, and increases its activity with increasing or decreasing visual flow speed, respectively (Fig. 6d,e). Similarly, values of θ close to 90º or 270º indicate that a bouton selectively carries running speed information and is positively (90º) or negatively (270º) correlated with running speed. Values in-between signify boutons carrying both visual flow and running speed signals, with θ close to 45º and 225º indicating cooperative interactions and θ close to 135º and 315º opposing interactions, with inverse activity-speed relationships for visual flow and running speed (Fig. 6d,e). Strikingly, a much larger proportion of LP than dLGN boutons showed such opposing interactions (Fig. 6e; LP: 28%, dLGN: 9%; $P < 10^{-10}$, Z test; see Methods). Conversely, boutons with cooperative interactions were more prevalent in dLGN (Fig. 6e; LP: 20%, dLGN: 27%; $P = 10^{-6}$, Z test). Moreover, a larger proportion of LP than dLGN boutons increased their activity with decreasing visual flow speed (Fig. 6e, LP: 17%, dLGN: 3%; $P < 10^{-10}$, Z test). Varying the PP threshold yielded very similar results (Supplementary Fig. 10e).

The difference in sensorimotor integration by dLGN and LP projections was also evident when comparing visual flow and running speed tuning curves of individual boutons (Fig. 6f). The speed tuning curves of many LP boutons were anti-correlated (Fig. 6f, left top). In contrast, proportionally more dLGN boutons tended to have tuning curves with similar shapes for visual flow and running speed (Fig. 6f, left bottom; Fig. 6f, median corr. coeff., dLGN: 0.28 ± 1.4, LP: −0.26 ± 1.7; $P = 10^{-10}$, Wilcoxon rank-sum test).

As a consequence of the opposing effects of running and visual flow speed on their responses, LP boutons are expected to exhibit activity related to the instantaneous difference between running and visual flow speed when these are uncoupled in the ‘open-loop’ condition. This difference signal may be highly relevant for visual processing because in principle, it enables the detection of discrepancies between the visual feedback expected from the animal’s locomotion and the actual visual input. Indeed, many boutons were more informative about the difference between running and visual flow speed than about either speed alone (random forests decoder, Fig. 7a-d). Boutons that preferentially signaled the degree of difference between running and visual flow speed were much more prevalent in LP than in dLGN projections (Fig. 7c,d; mean proportions, LP: 11 ± 1.5%, dLGN: 4.7 ± 0.7%; P = 0.0036, Wilcoxon rank-sum test; see Methods). Conversely, the proportion of boutons that were most informative about an equally weighted sum of running and visual flow speed was much larger in dLGN than in LP projections (Fig. 7c,d; mean proportions, dLGN: 7.2 ± 1.1%, LP: 3.0 ± 0.6%; P = 0.0004, Wilcoxon rank-sum).

Boutons signalling the degree of difference between running and visual flow speed showed increased activity with larger visuo-motor divergences (Supplementary Fig. 9e). Moreover, these boutons signaling visuo-motor discrepancies were less active in the ‘closed-loop’ condition, when running and visual flow were coupled, as no visuo-motor discrepancies occurred in these trials (Fig. 7e, mean change in activity, dLGN: −10.2 ± 1.9%, $P < 10^{-10}$; LP: −4.5 ± 1.9%, P = 0.0006; Wilcoxon signed-rank test). The activity of boutons most informative about the equally weighted sum of running and visual flow speed was not significantly changed when running and visual flow speed were coupled (Fig. 7e, mean

change in activity, dLGN: 2.1 ± 1.5%, P = 0.67; LP: 0.2 ± 2.1%, P = 0.96; Wilcoxon signed-rank test).

Interestingly, LP boutons on the whole were more active in response to an onset of visuomotor divergence than during a period of varying but sustained visuomotor discrepancies (mean difference in activity, LP: 30 ± 7%; P = 10^{-4}, Wilcoxon signed-rank test). This was not the case for dLGN boutons (mean difference in activity, dLGN: 6 ± 8%; P = 0.55, Wilcoxon signed-rank test), supporting the hypothesis that LP specifically might play a role in signalling unexpected visual motion.

In summary, both dLGN and LP projections to V1 signal information related to an animal's movement through the visual environment. Neurons in both thalamic nuclei integrate motor information about the speed of locomotion and sensory information about the speed of visual flow. However, while positive combinations of running and visual flow speed were enriched in dLGN boutons, boutons from higher-order nucleus LP predominantly conveyed the difference between self-generated and external visual motion.

Discussion

In this study, we reveal that the inputs from first-order and higher-order visual thalamus are functionally highly diverse and provide multiple visual, motor and visuomotor signals into L1 of mouse V1. Therefore, thalamic input not only provides feed-forward information about the sensory input but also rich contextual signals about the interaction of the animal with its environment.

Visual response properties

Cortical L1 receives prominent input from multiple thalamic nuclei29. In mouse V1, these include not only neurons in nucleus LP but also L1-projecting neurons located in the dorsal shell of dLGN, which might represent a pathway that is functionally distinct from the main dLGN input into L429–31. Even though L1-targeting projections from both dLGN and LP likely originate from so-called matrix-type thalamic neurons, which are thought to be topographically 'nonspecific' and diffuse29, they contribute fundamentally different visual information to V1. The properties of the small spatial receptive fields we observed in dLGN boutons were similar to that of the general dLGN neuronal population assessed with electrophysiological recordings and imaging techniques, including the degree of orientation and direction selectivity33,38–41. A subset of boutons was sharply tuned for orientation and/or direction, as described previously30. Surprisingly, dLGN inputs into L1 were retinotopically highly confined and topographically ordered, indicating that dLGN axons provide spatially organized information from restricted regions in visual space even in L1. In contrast, although the anatomy of LP projections was coarsely topographic in V1, the spatial receptive fields of LP inputs were much larger and emanated from widely dispersed locations in the visual field. This suggests that LP inputs provide contextual information about the visual scene, which extends far beyond the retinotopic preferences of local V1 neurons. LP inputs may therefore contribute to surround modulation of V1 neurons24, or to state-dependent or behavioral modulation of visual responses across visual space (see below).

Motor-related information

By measuring the thalamic input to V1 in mice experienced in traversing a virtual corridor, we found that L1-targeting projections from dLGN and LP signal rich information related to an animal's movement through the visual environment. Locomotion has been shown to influence responses in mouse V14–6. Current models suggest that locomotion signals are generated by neuromodulatory mechanisms of disinhibition acting directly in the cortical circuit11,12. However, we found that excitatory projections into V1 from dLGN and LP are strongly modulated by the behavior of the animal, including inputs carrying specific information about saccades and running speed. Our results are in agreement with electrophysiological evidence for running modulation of responses in mouse dLGN14. These motor signals could be inherited from the superior colliculus – a structure contributing to head and eye-movements26 as well as to modulation of locomotion in mice42 – which targets LP and the L1-projecting dorsal shell of dLGN31. Alternatively, locomotor signals in the thalamus could arise from cortico-thalamic feedback or from substantial neuromodulatory projections43,44. Irrespective of their source, the existence of motor signals in dLGN and LP indicate that the visual thalamus likely contributes to the running modulation of V1 responses.

Sensorimotor interaction signals

What role could motor signals play in the early visual system? They could be combined with visual motion signals to update an estimate of the animal's own speed through the environment. Indeed, a recent study revealed that a significant percentage of neurons in mouse V1 respond to positively weighted combinations of optic flow and running speed6. We find that this positive integration of visual and motor signals is already apparent at an even earlier visual processing stage, in the dLGN, while it is much rarer in higher-order nucleus LP. Interpreting the input from the visual environment in the context of how fast the animal moves may be important for navigation and generating internal representations of space45.

On the other hand, running speed and visual motion signals could be used to detect external visual motion independent of the visual motion generated by the animal's' own movements. By computing the difference between the actual optic flow speed and the speed predicted by the animal's locomotion (potentially based on an efference copy of the executed motor command), neurons would report instances of visuomotor mismatch. Indeed, such mismatch selective neurons have been observed in mouse V15. We find that signals reporting discrepancies between optic flow and running speed are also represented at the level of the thalamus, being particularly enriched in LP projections targeting V1.

The theoretical framework of predictive coding suggests that sensory neurons report the difference between their bottom-up inputs and top-down predictions of these inputs8,7,46. Sensorimotor mismatch signals are computationally and ethologically useful because they can serve as an error signal which signifies that the intended motor action did not result in the expected sensory feedback. These error signals may help to update intended movement plans and coordinate visually-guided behaviours, for which the pulvinar has been implicated19. In addition, activity reporting sensorimotor discrepancies may alert the animal

to unpredicted or unexpected sensory signals in the visual scene and allow for their processing independent from self-generated sensory input. Our results suggest that higher-order visual thalamus is part of a predictive coding circuit48 that integrates visual and motor information to calculate divergences between actual and expected visual feedback, and which therefore signals unpredicted visual motion. It remains to be determined whether these signals are computed within the thalamus itself, from separate inputs carrying optic flow and run speed information, or inherited from the mismatch neurons in the cortex5.

Irrespective of how discrepancy signals are generated in individual LP neurons, they are likely to be broadcast widely. Since LP boutons have large receptive fields and weak orientation selectivity, this nucleus might not compute and convey the precise properties of unpredicted visual stimuli; these are more likely to be processed in cortical visual areas5. Higher-order visual thalamus might instead be important for targeting attention to incongruent self-generated and external visual motion, for example when there is an object moving in the visual scene. Consistent with previous models, the pulvinar/LP could increase the saliency of such objects, for instance by coordinating activity across visual cortical areas and thereby facilitating information flow related to unpredicted visual motion through the cortical processing hierarchy23,26,47.

Impact on cortical circuits

Cortical layer 1 receives both thalamic inputs and cortical feedback projections which synapse onto inhibitory cell classes as well as the distal dendrites of pyramidal cells in this layer49. Nevertheless, these inputs can have a strong influence on neuronal activity, for instance by triggering active dendritic events when these coincide with the feed-forward activation of the cell24,50. Cortical feedback into layer 1 is thought to transmit internal, contextual information, and to provide predictions for the interpretation of sensory input3,50. Here we show that the signals from the visual thalamus, in addition to carrying specific signals about the speed of locomotion that might be considered predictive of imminent optic flow, also carry discrepancy signals that reflect the deviation from these visuomotor predictions. Future experiments are required to determine how different cell classes integrate these complex visuomotor signals to inform visual processing in thalamo-cortical loops.

Online methods

Surgical procedures

All experiments were conducted in accordance with the institutional animal welfare guidelines and licensed by the UK Home Office and the Swiss cantonal veterinary office. Animals used in this study were at least 6 weeks old C57BL/6 mice of either sex (anaesthetised recordings: 24 mice, awake recordings: 18 mice, anatomy: 7 mice). Prior to surgery, the animals were injected with dexamethasone (2–3 mg kg^{-1}), atropine (0.05–0.1 mg kg^{-1}) and analgesics (carprofen; 5 mg kg^{-1}). General anesthesia was induced with a mixture of fentanyl (0.05 mg kg^{-1}), midazolam (5 mg kg^{-1}), and medetomidine (0.5 mg kg^{-1}). For anatomical tracing, injections of fluorescent conjugate Cholera Toxin B (CTB; recombinant cholera toxin subunit B conjugated with Alexa fluorophores; 0.2% CTB488,

CTB555 and/or CTB647; Life Technology) were injected individually, or mixed with AAV2.1 Ef1a-eGFP or AAV2.1 Ef1a-tdTomato (1:4 dilution) using a glass pipette and a pressure injection system (Picospritzer III; Parker) either into the primary visual cortex (V1) based on intrinsic imaging maps (see below) or into LP based on stereotaxic coordinates (stereotaxic coordinates were adjusted depending on the age and weight of the animal and ranged from: −1.45 to −2.1 mm posterior to bregma, 1.4–1.45 mm lateral to bregma and 2.55–2.7 mm deep from cortical surface).

For anaesthetized and awake two-photon imaging, injections of AAV1.hSyn.GCaMP5G.WPRE.SV4051, AAV1.Syn.GCaMP6m.WPRE.SV40 or AAV1.Syn.GCaMP6f.WPRE.SV4034 (Penn Vector Core; dilution 1:2 to 1:10 in saline solution) into the right dLGN (stereotaxic coordinates ranged from: −2.0 to −2.6 mm posterior to bregma, 2.25–2.4 mm lateral to bregma and 2.55–2.7 mm deep from cortical surface), the right LP or right V1 were made using a glass pipette and a pressure injection system (Picospritzer III, Parker). All results in anaesthetised and awake recordings were similar for the different GCaMP variants used, therefore data were pooled. For imaging, a craniotomy of 4–5 mm diameter was made over right V1. The craniotomy was sealed with a glass cover slip and cyano-acrylic glue (UltraGel; Pattex) and a head-plate was attached to the skull using dental cement (Heraeus Sulzer or C&B). Animals were given antibiotic and analgesic drugs (enrofloxacin 5 mg kg^{-1}, buprenorphine 0.1 mg kg^{-1}) at the end of surgery and repeatedly during recovery. Imaging started approximately two to three weeks after the virus injection. At the end of the experiment, each mouse was euthanized and perfused transcardially, first with saline solution (NaCl, 0.9%) and then with 4% paraformaldehyde in PB. Relevant parts of the fixed brains were sectioned for histological processing (see below for details). Data collection was not performed blind to the conditions of the experiment. No sample size calculation was performed but sample sizes are consistent with those generally employed in the field.

Intrinsic signal imaging

To determine the detailed location and organization of primary visual cortex for retinotopic injections of CTB, mice underwent optical imaging of intrinsic signals. Two to three days prior to imaging, mice underwent surgeries as described above. A customized headplate was implanted and the skull was carefully thinned to improve the quality of imaging. On the day of imaging, mice were initially sedated (Chlorprothixene, 0.7 mg kg^{-1}) then lightly anesthetized with isoflurane (0.5–1% in O2) delivered via a nose cone. Visual cortex was illuminated with 700 nm light split from an LED source into 2 light guides. Imaging was performed with a tandem lens macroscope focused 500 μm below the cortical surface and a bandpass filter centered at 700 nm with 10 nm bandwidth (67905; Edmund optics). Images were acquired with a rate of 6.25 Hz with a 12 bit CCD camera (1300QF; VDS Vosskühler), frame grabber (PCI-1422; National Instruments) and custom software written in Labview (Texas Instruments). The visual stimulus was a white bar 3–4 degrees in width, which drifted left, right, up or down at 0.09 Hz on a black background. Intrinsic signals maps were obtained by determining the temporal phase of the Fourier component at the frequency of the drifting bar. To obtain the retinotopic maps shown in Supplementary Fig. 2, the

responses for both directions of the drifting bar were averaged and thresholded by the normalized power map of the corresponding trial.

Histology and Confocal Imaging

After perfusion of the animal, the brain was embedded in 4% agar (A9539; Sigma) and slices were cut at a thickness of 100–150 μm using a vibratome (HM650V; Microm). Slices were counterstained either by mounting them in a mouting medium countaining DAPI (Vectashield; Vector Laboratories) or by Nissl staining (NeuroTrace™ 435/455, 1:50 dilution; Molecular Probes) before mounting them with a hard-set mounting medium (2.5% DABCO (D27802; Sigma), 10% polyvinyl alcohol (P8136; Sigma), 5% glycerol, 25mM Tris buffer pH 8.4). Images of either 512 × 512 pixels or 1024 × 1024 pixels were acquired with a confocal microscope (Zeiss point scanning confocal, LSM700 inverted) using a 10× or 25× objective.

Two-photon calcium imaging and visual stimulation

Anaesthetized experiments—Imaging in anesthetized animals was performed with a custom galvo-scanning two-photon microscope and a mode-locked Ti:sapphire laser (Mai Tai; SpectraPhysics) at 930 nm through a 40× water immersion objective (0.8 NA; Olympus). Scanning and image acquisition were controlled by custom software written in Labview (Texas Instruments). Frames of 256 × 256 pixels with a field of view of 120 × 120 μm (bouton imaging) or 250 × 250 μm (cell body imaging) were acquired at a rate of ~3.8 Hz. Visual stimuli were generated in Matlab using Psychophysics Toolbox52 and presented on an LCD monitor (60 Hz refresh rate) positioned 20 cm from the left eye, at approximately 45 degrees of the long axis of the animal such that it covered ~105 × 85 degrees of visual space. Squarewave gratings (0.04 cycles per degree, 2 Hz, 100% contrast) drifting in 12 different directions for 2 s were presented randomly interleaved with a gray screen (~4.2 s) between grating presentations. Each grating direction was repeated 8 times. A subset of LP data was obtained with a spatial frequency of 0.02 cycles per degree. The results for 0.02 and 0.04 were almost identical and not statistically significantly different and were therefore pooled. Receptive field mapping stimuli consisted of black and white squares of 8 × 8 degrees on a gray background. The squares were presented one at a time and in random order at one of 120 positions (12 × 10 matrix covering a total area of 96 × 80 degrees; each position was repeated 9–18 times). The presentation rate was ~1.9 Hz and the square presentation duration was ~0.52 s (equivalent to the duration of two imaging frames), i.e. there was no gap between presentations. For imaging, the mice were lightly anesthetized with chlorprothixene (0.7 mg kg^{-1}) and isoflurane (0.5–1% in O2). Atropine was given to slightly dilate the pupil and reduce mucus secretion. Eyes were covered with eye ointment (Maxitrol), reduced to a thin layer during imaging. The ipsilateral eye was covered. Rectal temperature was kept constant at 37°C with the help of a heating pad (DC Temperature Controller; FHC).

Awake experiments—Mice were housed with an inverted light-dark cycle from at least five days prior to the first imaging experiments. All experiments were performed during the dark phase. Animals were handled and accustomed to head-restraint for 3–5 days. Imaging was performed using a commercial resonant scanning two-photon microscope (B-Scope;

Europe PMC Funders Author Manuscripts

Thorlabs) and a Spectra Physics MaiTai DeepSee laser (SpectraPhysics) at 960 nm with a 16× water immersion objective (0.8 NA; Nikon). Images of 512 × 512 pixels with fields of view ranging from 180 × 180 μm to 100 × 100 μm were acquired at a frame rate of 30 Hz using ScanImage 4.153. The power supply of the monitor back-light was controlled using a custom-built circuit54 to present visual stimuli only in-between the scanning of two subsequent lines. During recordings, mice were free to run on a 20 cm diameter styrofoam cylinder. Their running speed was measured with an optical mouse (Logitech G700). This signal was used to control the speed at which mice moved through a virtual environment that was presented on two monitors (U2312HM; Dell) in front of them. The virtual environment consisted of linear corridors with varying wall patterns as described previously55 (gratings and black and white circles on a gray background) created in a game engine (Unity), and the position in the environment was controlled by custom software written in Labview (National Instruments). These 'closed-loop' recordings, in which the running of the mouse controlled the visual flow of the virtual corridor, were alternated with recordings during which animals ran in the dark (monitors were switched off), and with 'open-loop' recordings during which visual flow presented to the mouse was not coupled to the running of the animal, but was a replay of a previous recording. For the analysis presented in this manuscript, we only included recordings during which mice ran regularly at maximum speeds >= 10 cm s^{-1}. This ensured that only recordings in which animals were habituated and familiar with the virtual environment were included for further analysis. Images of both eyes were recorded with CMOS cameras at 30 Hz (DMKBUC03, Imaging Source). Pupil position was computed offline by smoothing and thresholding the images and fitting a circle to the pupil. The filter radius and the image threshold were adapted manually for each experiment. We applied a one-dimensional median filter to the traces of horizontal and vertical pupil position. Eye movements were detected automatically by applying an adapted threshold which had to be passed in the horizontal, but not the vertical plane. This criterion avoided detecting artifacts due to blinking or grooming and led to few missed saccades. While the occurrence of events was determined using the filtered traces, event timing was corrected using the raw traces. This method was cross-validated in several experiments using manual detection of eye movements.

Data Analysis

Anaesthetized experiments—All analyses were performed in Matlab (Mathworks). Image stacks were registered56 to a 30 frame average to correct for x-y motion. Regions of interest (ROIs) corresponding to cell somata were determined manually on the basis of frame averages and inspection of movies of calcium activity. ROIs corresponding to putative boutons were selected in an automated procedure. An adaptive local threshold was applied to an image in which each pixel represented the average temporal cross correlation with its eight neighbors57. The resulting ROI masks were visually inspected and, if necessary, pixels corresponding to stretches of axons were manually removed. All pixels within each ROI were averaged to give a single time course. Calcium $\Delta F/F$ signals were obtained by using the median between the 10th and 70th percentile over the entire fluorescence distribution as F_0. This trace was high-pass filtered at a cut-off frequency of 0.02 Hz to remove slow fluctuations in the signal. Only ROIs with clear visually-evoked calcium transients were analyzed: for grating stimuli these were defined as ROIs that showed a significant calcium

response (average $\Delta F/F$ during the grating presentation) to at least one grating direction relative to the gray screen (one-way ANOVA, $P < 0.0001$) and whose average response to their preferred grating direction was at least 0.5 $\Delta F/F$. The orientation selectivity index (OSI) was defined as $(R_{pref} - R_{ortho})/(R_{pref} + R_{ortho})$, where R_{pref} is the response to the preferred direction and R_{ortho} is the average of the responses to the directions orthogonal to the best direction. DSI was defined as $(R_{pref} - R_{opp})/R_{pref} + R_{opp}$ where R_{opp} is the response to the direction opposite the preferred direction.

ON and OFF spatial receptive fields (RFs) were derived separately by analyzing only responses to the white patches or only responses to the black patches, respectively. Raw RFs represent the mean response at each of the 12 × 10 stimulus positions. A response was defined as the mean $\Delta F/F$ within a window of 2 frames. The first frame that passed a one-way ANOVA across the 120 stimulus positions ($P < 0.0005$) was the first frame of the response window. ROIs that did not pass this test within the first four frames after stimulus onset or whose strongest mean response was < 0.5 $\Delta F/F$ were excluded. If the ROI passed the test for both the black (OFF) and white (ON) patches but with different latencies only the RF type with the shorter latency was included for further analysis. The raw RF was interpolated at one degree resolution and smoothed with an 11 × 11 degrees square filter before being thresholded at the half maximum response. In the rare cases where more than one region remained after this step, all but the one containing the strongest average response were removed. This thresholded RF subdomain was used to derive parameters such as RF area and centroid for all further analyses. RF scatter was computed by measuring the distance between all combinations of pairs of RF subdomain centroids within an imaging region. Computing RF scatter using the center of mass of the combined RF for neurons or boutons with both an ON and an OFF subdomain yielded identical results. Visual field coverage represents the area of the visual field that is covered by the entire population of RFs within an imaging area. To assess how the visual field coverage increases as a function of the number of RFs within an imaged region, we randomly drew one RF after the other from the population of RFs within a region, measured the visual field coverage after each newly added RF, repeated this procedure 100 times, and plotted the average visual field coverage as a function of the number of RFs. To examine the retinotopic organization of thalamic boutons and V1 neurons we correlated the RF positions (separately for elevation and azimuth) with the location of the ROI in cortical space on a series of axes spanning 360° at 1° intervals. For ROIs with both ON and OFF RF subdomains the average position of the two was taken. The direction with the maximum correlation between RF positions and cortical position of the ROIs of all boutons was taken as the direction of the retinotopic gradient for azimuth and elevation, respectively. For multiple comparisons, a Kruskal-Wallis test was followed by Wilcoxon rank-sum tests. Reported P-values are Bonferroni-corrected.

In addition to the analysis of visual response properties based on individual boutons or receptive fields, we also carried out a region-based analysis in which each imaged region contributes only a single data point, the median value of all boutons in the imaged region. In the region-based analysis all averages lay within 10% of the reported results and all reported dLGN vs LP differences were also found to be statistically significant at $P < 10^{-4}$.

Awake experiments—All analyses were performed in Matlab (Mathworks). Image stacks were registered56 to a 30 frame average to correct for x-y motion. Frames with large motion artefacts often due to grooming were detected by inspecting the x-y displacement obtained by registration and were subsequently removed from analysis. Regions of interest (ROI) corresponding to putative axonal boutons were detected semi-automatically using intensity thresholding combined with PCA-ICA refinement58 and were inspected manually. In experiments where the same boutons were imaged over several conditions, ROIs were selected from a combined time-averaged image stack. Calcium $\Delta F/F$ signals were obtained by using the 25th percentile over the entire fluorescence distribution as F_0. To identify responsive ROIs, we measured the skewness of $\Delta F/F$ values of individual ROIs over the recording. ROIs with skewness > 1 were considered to be responsive. For calculating the difference in activity between open-loop and closed-loop trials for individual boutons (Fig. 7e), $\Delta F/F$ traces were thresholded at 3.29 times the standard deviation (0.1% of values outside the confidence interval) above the 50th percentile and data points below were set to zero. For this analysis, recordings and average image stacks were manually inspected, and experiments with any positional drift of the imaging region between recordings of the same boutons were excluded.

Firing rates per imaging frame were inferred from calcium transients using a compressive sensing technique59. Parameters for baseline calcium transient templates for GCaMP5 and GCaMP6f expressing boutons were estimated from published reports34,51, and modified as required through visual inspection of observed calcium signals. Baseline calcium templates were given by the function

$$C(t)=\begin{cases} min\left[1-exp\left(-\frac{t}{\tau_R}\right), exp\left(-\frac{t-t_P}{\tau_{F1}}\right)\right], t \le t_{FI} \\ exp\left(-\frac{t-t_{FI}}{\tau_{F2}}\right) exp\left(-\frac{t-t_P}{\tau_{F1}}\right), t > t_{FI} \end{cases}$$

Parameters for the various indicators were given by $\Phi = \{\tau_R, t_P, \tau_{F1}, t_{FI}, \tau_{F2}\}$: $\Phi_{GCaMP5,bouton}$={50 ms, 170 ms, 450 ms, 500 ms, 600 ms}; $\Phi_{GCaMP6f,bouton}$={50 ms, 170 ms, 450 ms, 500 ms, 600 ms}.

To determine if a bouton was significantly modulated by the onset of a saccade-like eye movement (see above), we compared the average inferred firing rate 1.5–0.5 s before the event to the average inferred firing rate 0–1 s after the event using a Wilcoxon signed-rank test at a significance threshold of 1%.

Decoding analysis—We quantified the information contained in a single bouton response about a particular variable (running speed, RS, visual flow speed, VF, the difference between running speed and visual flow speed, RS−VF or their equally weighted sum, RS+VF) using random forests, a non-parametric machine learning algorithm, which forms ensembles of regression trees36,37. Random forest ensembles were trained using a bootstrap aggregation algorithm, using the Matlab Statistics Toolbox TreeBagger class (Mathworks). Each ensemble consisted of 32 regression trees, with a minimum of 5 observations per leaf node. Ensembles were trained to use inferred firing rates $x_i(t)$ of a single bouton i over a ±250 ms period to predict instantaneous speed, instantaneous RS−VF or instantaneous RS+VF,

denoted $y(t)$. All signals were binned at 50 ms; 10 time bins of inferred firing rate centered around zero were then used to compose a vector $X_i(t) = [x_i(t - 250\text{ ms}), x_i(t - 200\text{ ms}), \ldots, x_i(t + 250\text{ ms})]$; ensembles formed a non-linear mapping $X_i(t) \Rightarrow \hat{y}(t)$ while minimising the difference between the predicted and observed instantaneous speed, $\hat{y}(t) - y(t)$. Ensembles were trained under a cross-validation paradigm; each experimental session was partitioned into 80% training data and 20% testing data, repeated five times. The prediction power PP over the test set was measured as the Pearsons's correlation coefficient $PP = \text{corr}[y(t), \hat{y}(t)]$ between the predicted and observed variable over test samples, and averaged over the five test partitions.

We defined individual boutons as significantly conveying a particular signal when PP > 0.16 for that signal; we classified individual boutons as preferentially conveying a particular signal if the PP for that signal was higher than for any other signal, and if PP > 0.16 (Fig. 7). This threshold ensured that activity of the included boutons was highly significantly informative about the tested signal ($P < 10^{-4}$) and the influence of potential motion artifacts in the calcium signal was minimized: in animals in which LP was injected with AAV2.1-Ef1a-eGFP, and GFP-labelled LP boutons in V1 were imaged during the open-loop condition described above, only 4.6% GFP boutons passed the responsiveness criteria (skewness > 1, 368 out of 7977 boutons, 22 sessions, 4 mice). Of those boutons only few passed the decoding threshold PP > 0.16 (RS: 11%; VF: 0%; RS−VS: 0.5%; RS+VF: 0.8%), constituting less than 0.6% of total boutons that would be scored as significantly informative to any of the tested variables with our analysis. Moreover, 90% of these boutons had negative RS correlations, in clear contrast to calcium signals in both LP and dLGN boutons (LP: 25%; dLGN: 13% negative RS correlations). To test whether movement artifacts could lead to significant prediction power about running speed in active boutons with GCaMP calcium transients, we added surrogate calcium transients to the raw GFP fluorescent traces, modelled on the electrophysiological spike rates as well as the calcium transients observed in the bouton calcium traces of our GCaMP data set. Spikes were drawn from a bursty Poisson distribution (5 Hz average rate for initial distribution, followed by 50% burst probability per spike) and convolved with a calcium transient (amplitude 40% $\Delta F/F$; other parameters as for GCaMP6f described above). We then performed spike estimation and single-bouton decoding on the surrogate traces, as described above. A very small minority of surrogate bouton signals passed the PP threshold of 0.16 (RS: 0.19%; VF: 0%; RS−VF: 0.02%; RS+VF: 0.02% of boutons; c.f. Fig. 6c and Fig. 7d), indicating that potential movement artifacts in the calcium data do not contribute to the presented results. Differences between LP and dLGN boutons described in the manuscript were robust over a wide range of PP thresholds (see Supplementary Fig. 10e).

To compare bouton responses to the onset of RS and VF divergences with responses during periods of sustained divergence, we identified continuous periods of low and high absolute RS−VF (less and more than 2 cm s^{-1} of absolute RS−VF difference, respectively). We then compared the average inferred spikes during a 1s window following RS−VF divergence onset following at least 2 s of low absolute RS−VF, with a 1 s window of high absolute RS −VF at the ends of stretches of high absolute RS−VF of at least 2 s duration, for each bouton.

Tuning curve quantification and analysis—We estimated tuning curves using a kernel density estimate of the inferred firing rate $x_i(t)$ of a bouton i, for a given speed $y(t)$.

Estimates were computed using a Gaussian window with standard deviation $\sigma=2\kappa(\frac{4}{3\#[Y]})^{\frac{1}{5}}$ over a given speed $y(t)$, where κ = median$_t$[*abs* $y(t)$ − median$_t${$y(t)$}]; median$_t$[$y(t)$] denotes the median value of $y(t)$, computed over all time samples t; and #[Y] gives the number of samples in the time series $y(t)$. Tuning curves were divided into twelve bins over speed values, with equal numbers of samples per bin. For running speed and visual flow speed, the first bin consisted of values < 3cm s^{-1} (the "stationary" bin), and was ignored for determining the significance of tuning curves. Significant modulation of inferred firing rate by specific non-stationary speeds was determined by comparing mean inferred firing rates per bin against a monte-carlo bootstrap resampling of inferred firing rates, with multiple-comparisons correction over speed bins60.

Tuning curves that contained significant bins (for speeds > 3 cm s^{-1}), were classified into three broad categories: increasing or decreasing activity with increasing speed, and speed band-preference (encompassing band-pass and band-cut). Tuning curves were divided into thirds over the whole range of speeds, such that each third contained four speed bins. If at least one bin within a third showed significant positive or negative modulation, then that third was considered significantly positively (1) or negatively (−1) modulated, respectively. The pattern of modulation over these thirds was used to classify the shape of the tuning curve. Tuning curves with patterns [0 0 1, −1 0 1, −1 −1 1, 0 −1 1, −1 −1 0, 0 1 1, −1 1 1, −1 0 0] were classified as increasing; tuning curves with patterns [1 0 0, 1 0 −1, 1 −1 −1, 1−1 0, 0 −1 −1, 1 1 −1, 1 1 0, 0 0 −1] were classified as decreasing; tuning curves with patterns [0 1 0, −1 1 0, 0 1 −1, −1 1 −1, −1 0 −1, 0 −1 0, 1 0 1, 1 −1 1] were classified as band-preference.

Interaction angle—An interaction angle θ between RS and VF PP of the random forests decoder was computed for individual boutons (Fig. 6e; Fig. 7c). First, a "signed" PP measure was determined by modifying the decoding PP for each bouton as follows. The sign of the Pearson's linear correlation coefficient between inferred firing rate and RS or VF (zero lag) was assigned as the sign of the PP. Accordingly, boutons whose activity showed a positive correlation with RS or VF had positive PPs for these variables, while boutons which were negatively correlated with RS or VF had negative PPs. The interaction angle θ was then computed as θ = atan(*signed* PP_{RS}/*signed* PP_{VF}).

In order to avoid distorting the circular distribution of θ, decoding PP thresholds were applied as follows when calculating circular distributions of interaction angles. The magnitude of the vector composed by [PP_{VF}, PP_{RS}] was computed as $|PP|=\sqrt{PP_{RS}{}^2+PP_{VF}{}^2}$. Only boutons with |PP| > 0.16 were included in the analysis. The proportions of boutons with opposing interactions between RS and VF (Fig. 6e) were defined as the numbers of boutons with interaction angles θ within 45º-wide bins centered around 135° and 315° over all boutons with |PP| > 0.16. Proportions of boutons with cooperative interactions between RS and VF (Fig. 6e) were defined as numbers of boutons with θ within 45º-wide bins centered around 45° and 225° over all boutons with |PP| > 0.16.

For comparison, the interaction angle was determined using linear correlation coefficients (Supplementary Fig. 10). Pearson's linear correlation coefficients were measured between the activity of a single bouton and either running speed (R_{RS} = corr[$x_I(t)$, $y_{RS}(t)$]) or visual flow speed (R_{VF} = corr[$x_I(t)$, $y_{VF}(t)$]), with all signals binned at 50ms, and with zero relative lag between signals. A linear interaction angle θ_{lin} was computed as θ_{lin} = atan(R_{RS}/R_{VF}). Proportions of boutons conveying RS and VF speed interactions were computed as above.

Electrophysiological recordings

Electrophysiological recordings were performed on 8 male C57BL/6j mice (age 2–3 months). Mice were anaesthetized and prepared for stereotaxic surgery as described above. A small (~1–2 mm) craniotomy and a durectomy was performed on the right hemisphere guided by stereotaxic coordinates, 1.6–1.9 mm lateral and 2.2 mm posterior to Bregma. During recordings anaesthesia was maintained with isoflurane (0.5–1% in O_2). Dehydration of the exposed cortical surface was prevented by regular administration of cortex buffer (125 mM NaCl, 5 mM KCl, 10 mM HEPES, 2 mM Mg_2SO_4, 2 mM $CaCl_2$, 10 mM glucose, pH 7.4). The ipsilateral eye was covered to prevent binocular stimulation. Neural activity was recorded using silicon multisite electrodes arranged in an eight-tetrodes configuration (A4 × 2-tet-10mm-150-200-121, NeuroNexus Technologies) coated with DiI (Invitrogen; Life Technologies). Electrodes were lowered to approximately 2.5–3.2 mm below the cortical surface. Positions were confirmed by monitoring responses to 200 ms light flashes. Signals were acquired at 25 kHz using a System 3 workstation (Tucker-Davis Technologies), threshold crossings were detected offline by SpikeDetekt and auto clustered using KlustaKwik followed by manual adjustment using KlustaViewa61. Single-units were further analysed with custom software in Matlab (MathWorks). Only units exhibiting a clear refractory period (>1.5 ms) and stable amplitude and waveform were considered for analysis.

Visual stimuli consisted of 8 × 8 degrees black and white squares on a grey background presented randomly at 12 × 10 positions on the monitor. Black or white squares were either presented separately, randomly interleaved, for 0.3 s every 0.5 s, or alternated 4 times within 0.8 s (each stimulus duration 0.2 s) every 1 s. For quantifying receptive field size only responses to alternating stimuli were included since all dLGN units were recorded using this protocol. Visually-evoked firing rate and response latency were similar with both protocols and data were pooled. Receptive fields were calculated as described above from the average firing rate 50 ms after stimulus onset to 50 ms after stimulus offset. Response latency was determined from 5 ms bins and was defined as the first of two consecutive bins that exceed the 95% confidence limit of the pre-stimulus (200 ms) firing rate.

At the end of each experiment, the brain was removed and fixed in 4% paraformaldehyde in PBS overnight. Brains were sliced (150 μm) with a vibratome, mounted and visualised under a fluorescent stereo microscope (Zeiss Lumar.V12) to reconstruct the position of recording sites. Images were scaled to account for fixation and/or mounting artefacts based on a stereotaxic atlas62 using hippocampus, midline and thalamic borders as landmarks. Anatomical locations of recording sites were then estimated based on the fluorescent track of the electrode shanks, the recording depth and the defined geometry of the electrode array.

Boundaries of dLGN were clearly visible from tissue landmarks. Borders of LPrm (lateral posterior nucleus, rostro-medial section) and LPl (lateral posterior nucleus, lateral section) are diffuse and were estimated based on stereotaxic atlas coordinates62.

Two-sided statistical tests were used for all analyses, unless specified otherwise. A supplementary methods checklist is available.

Supplementary Material

Refer to Web version on PubMed Central for supplementary material.

Acknowledgements

We thank Jasper Poort and Adil G. Khan for generous help, software and hardware for the behavioral experiments, data acquisition and analysis, Ho Ko for analysis software, Marius Pachitariu for related preliminary analysis, Abdel Nemri for building the intrinsic imaging setup, Georg B. Keller and his group for analysis software and AAV vectors, and Ivana Orsolic for an earlier version of the schematic in Fig. 5a. We thank Petr Znamensky, Jasper Poort, Antonin Blot, Andreas J. Keller and Georg B. Keller for comments on earlier versions of the manuscript, the Hofer and Mrsic-Flogel lab for discussions and Thomas D. Mrsic-Flogel for support, comments and discussions. We thank the Biozentrum Imaging Core Facility (IMCF; Basel) for providing access and maintenance of confocal microscopes as well as analysis support. We thank the GENIE Program, Janelia Farm Research Campus, Howard Hughes Medical Institute for making GCaMP5 and 6 material available. This work was supported by the European Research Council (SBH, HigherVision 337797) and the Wellcome Trust (SBH, 095853, JCD, 076508).

References

1. Gilbert CD, Wiesel TN. The influence of contextual stimuli on the orientation selectivity of cells in primary visual cortex of the cat. Vision Res. 1990; 30:1689–1701. [PubMed: 2288084]
2. Roelfsema PR, Lamme VAF, Spekreijse H. Object-based attention in the primary visual cortex of the macaque monkey. Nature. 1998; 394:287–291. [PubMed: 9685160]
3. Gilbert CD, Li W. Top-down influences on visual processing. Nat Rev Neurosci. 2013; 14:350–363. [PubMed: 23595013]
4. Niell CM, Stryker MP. Modulation of Visual Responses by Behavioral State in Mouse Visual Cortex. Neuron. 2010; 65:472–479. [PubMed: 20188652]
5. Keller GB, Bonhoeffer T, Hübener M. Sensorimotor mismatch signals in primary visual cortex of the behaving mouse. Neuron. 2012; 74:809–15. [PubMed: 22681686]
6. Saleem, aB, Ayaz, a, Jeffery, KJ., Harris, KD., Carandini, M. Integration of visual motion and locomotion in mouse visual cortex. Nat Neurosci. 2013; 16:1864–1869. [PubMed: 24185423]
7. Mumford D. On the computational architecture of the neocortex. Biol Cybern. 1992; 66:241–251. [PubMed: 1540675]
8. Rao RPN, Ballard DH. Predictive coding in the visual cortex: a functional interpretation of some extra-classical receptive-field effects. Nat Neurosci. 1999; 2:79–87. [PubMed: 10195184]
9. Makino H, Komiyama T. Learning enhances the relative impact of top-down processing in the visual cortex. Nat Neurosci. 2015; 2015
10. Zhang S, et al. Long-range and local circuits for top-down modulation of visual cortex processing. Science. 2014; 345:660–665. [PubMed: 25104383]
11. Lee, aM, et al. Identification of a brainstem circuit regulating visual cortical state in parallel with locomotion. Neuron. 2014; 83:455–466. [PubMed: 25033185]
12. Fu Y, et al. A cortical circuit for gain control by behavioral state. Cell. 2014; 156:1139–1152. [PubMed: 24630718]
13. McAlonan K, Cavanaugh J, Wurtz RH. Guarding the gateway to cortex with attention in visual thalamus. Nature. 2008; 456:391–394. [PubMed: 18849967]
14. Erisken S, et al. Effects of Locomotion Extend throughout the Mouse Early Visual System. Curr Biol. 2014; 24:2899–2907. [PubMed: 25484299]

15. Williamson RS, Hancock KE, Shinn-Cunningham BG, Polley DB. Locomotion and Task Demands Differentially Modulate Thalamic Audiovisual Processing during Active Search. Curr Biol. 2015; 25:1885–1891. [PubMed: 26119749]
16. Sherman SM, Guillery RW. The role of the thalamus in the flow of information to the cortex. Philos Trans R Soc Lond B Biol Sci. 2002; 357:1695–1708. [PubMed: 12626004]
17. Shipp S. The functional logic of cortico-pulvinar connections. Philos Trans R Soc Lond B Biol Sci. 2003; 358:1605–1624. [PubMed: 14561322]
18. Grieve KL, Acuña C, Cudeiro J. The primate pulvinar nuclei: Vision and action. Trends Neurosci. 2000; 23:35–39. [PubMed: 10631787]
19. Saalmann YB, Kastner S. Cognitive and Perceptual Functions of the Visual Thalamus. Neuron. 2011; 71:209–223. [PubMed: 21791281]
20. Kaas JH, Lyon DC. Pulvinar contributions to the dorsal and ventral streams of visual processing in primates. Brain Res Rev. 2007; 55:285–296. [PubMed: 17433837]
21. Raczkowski D, Rosenquist AC. Connections of the multiple visual cortical areas with the lateral posterior-pulvinar complex and adjacent thalamic nuclei in the cat. J Neurosci. 1983; 3:1912–1942. [PubMed: 6619917]
22. Bender DB. Receptive-field properties of neurons in the macaque inferior pulvinar. J Neurophysiol. 1982; 48:1–17. [PubMed: 7119838]
23. Saalmann YB, Pinsk MA, Wang L, Li X, Kastner S. The Pulvinar Regulates Information Transmission Between Cortical Areas Based on Attention Demands. Science. 2012; 337:753–756. [PubMed: 22879517]
24. Purushothaman G, Marion R, Li K, Casagrande VA. Gating and control of primary visual cortex by pulvinar. Nat Neurosci. 2012; 15:905–12. [PubMed: 22561455]
25. Baldwin MKL, Wong P, Reed JL, Kaas JH. Superior colliculus connections with visual thalamus in gray squirrels (Sciurus carolinensis): Evidence for four subdivisions within the pulvinar complex. J Comp Neurol. 2011; 519:1071–1094. [PubMed: 21344403]
26. Wurtz RH, McAlonana K, Cavanaugh J, Berman RA. Thalamic pathways for active vision. Trends Cogn Sci. 2011; 15:177–184. [PubMed: 21414835]
27. Kamishina H, et al. Cortical connections of the rat lateral posterior thalamic nucleus. Brain Res. 2009; 1264:39–56. [PubMed: 19368845]
28. Gale SD, Murphy GJ. Distinct Representation and Distribution of Visual Information by Specific Cell Types in Mouse Superficial Superior Colliculus. J Neurosci. 2014; 34:13458–13471. [PubMed: 25274823]
29. Rubio-Garrido P, Pérez-de-Manzo F, Porrero C, Galazo MJ, Clascá F. Thalamic input to distal apical dendrites in neocortical layer 1 is massive and highly convergent. Cereb Cortex. 2009; 19:2380–95. [PubMed: 19188274]
30. Cruz-Martín A, et al. A dedicated circuit links direction-selective retinal ganglion cells to the primary visual cortex. Nature. 2014; 507:358–61. [PubMed: 24572358]
31. Bickford ME, Zhou N, Krahe TE, Govindaiah G, Guido W. Retinal and Tectal 'Driver-Like' Inputs Converge in the Shell of the Mouse Dorsal Lateral Geniculate Nucleus. J Neurosci. 2015; 35:10523–10534. [PubMed: 26203147]
32. Tohmi M, Meguro R, Tsukano H, Hishida R, Shibuki K. The extrageniculate visual pathway generates distinct response properties in the higher visual areas of mice. Curr Biol. 2014; 24:587–597. [PubMed: 24583013]
33. Piscopo DM, El-Danaf RN, Huberman AD, Niell CM. Diverse Visual Features Encoded in Mouse Lateral Geniculate Nucleus. J Neurosci. 2013; 33:4642–4656. [PubMed: 23486939]
34. Chen T-W, et al. Ultrasensitive fluorescent proteins for imaging neuronal activity. Nature. 2013; 499:295–300. [PubMed: 23868258]
35. De Paola V, et al. Cell type-specific structural plasticity of axonal branches and boutons in the adult neocortex. Neuron. 2006; 49:861–875. [PubMed: 16543134]
36. Petreanu L, et al. Activity in motor–sensory projections reveals distributed coding in somatosensation. Nature. 2012; 489:299–303. [PubMed: 22922646]

37. Huber D, et al. Multiple dynamic representations in the motor cortex during sensorimotor learning. Nature. 2012; 484:473–478. [PubMed: 22538608]
38. Grubb MS, Thompson ID. Quantitative characterization of visual response properties in the mouse dorsal lateral geniculate nucleus. J Neurophysiol. 2003; 90:3594–607. [PubMed: 12944530]
39. Marshel JH, Kaye AP, Nauhaus I, Callaway EM. Anterior-Posterior Direction Opponency in the Superficial Mouse Lateral Geniculate Nucleus. Neuron. 2012; 76:713–720. [PubMed: 23177957]
40. Zhao X, Chen H, Liu X, Cang J. Orientation-selective responses in the mouse lateral geniculate nucleus. J Neurosci. 2013; 33:12751–63. [PubMed: 23904611]
41. Scholl B, Tan AYY, Corey J, Priebe NJ. Emergence of orientation selectivity in the Mammalian visual pathway. J Neurosci. 2013; 33:10616–24. [PubMed: 23804085]
42. Liang F, et al. Sensory Cortical Control of a Visually Induced Arrest Behavior via Corticotectal Projections. Neuron. 2015; 86:755–767. [PubMed: 25913860]
43. Sillito AM, Cudeiro J, Jones HE. Always returning: feedback and sensory processing in visual cortex and thalamus. Trends Neurosci. 2006; 29:307–316. [PubMed: 16713635]
44. Mccormick DA. Neurotransmitter actions in the thalamus and cerebral cortex and their role in neuromodulation of thalamocortical activity. Prog Neurobiol. 1992; 39:337–388. [PubMed: 1354387]
45. Kropff E, Carmichael JE, Moser M-B, Moser EI. Speed cells in the medial entorhinal cortex. Nature. 2015; 523:419–424. [PubMed: 26176924]
46. Friston K. A theory of cortical responses. Philos Trans R Soc Lond B Biol Sci. 2005; 360:815–836. [PubMed: 15937014]
47. Robinson DL, Petersen SE. The pulvinar and visual salience. Trends Neurosci. 1992; 15:127–132. [PubMed: 1374970]
48. Guillery RW, Sherman SM. Branched thalamic afferents: What are the messages that they relay to the cortex? Brain Res Rev. 2011; 66:205–219. [PubMed: 20696186]
49. Harris KD, Mrsic-Flogel TD. Cortical connectivity and sensory coding. Nature. 2013; 503:51–8. [PubMed: 24201278]
50. Larkum M. A cellular mechanism for cortical associations: An organizing principle for the cerebral cortex. Trends Neurosci. 2013; 36:141–151. [PubMed: 23273272]
51. Akerboom J, et al. Optimization of a GCaMP Calcium Indicator for Neural Activity Imaging. J Neurosci. 2012; 32:13819–13840. [PubMed: 23035093]
52. Brainard DH. The psychophysics toolbox. Spat Vis. 1997:433–436. [PubMed: 9176952]
53. Pologruto, Ta, Sabatini, BL., Svoboda, K. ScanImage: flexible software for operating laser scanning microscopes. Biomed Eng Online. 2003; 2:13. [PubMed: 12801419]
54. Leinweber M, et al. Two-photon calcium imaging in mice navigating a virtual reality environment. J Vis Exp. 2014; 84:e50885–e50885.
55. Poort J, et al. Learning Enhances Sensory and Multiple Non-sensory Representations in Primary Visual Cortex. Neuron. 2015; 86:1478–1490. [PubMed: 26051421]
56. Guizar-Sicairos M, Thurman ST, Fienup JR. Efficient subpixel image registration algorithms. Opt Lett. 2008; 33:156–158. [PubMed: 18197224]
57. Smith SL, Häusser M. Parallel processing of visual space by neighboring neurons in mouse visual cortex. Nat Neurosci. 2010; 13:1144–9. [PubMed: 20711183]
58. Mukamel EA, Nimmerjahn A, Schnitzer MJ. Automated analysis of cellular signals from large-scale calcium imaging data. Neuron. 2009; 63:747–60. [PubMed: 19778505]
59. Dyer EL, Studer C, Robinson JT, Baraniuk RG. A robust and efficient method to recover neural events from noisy and corrupted data. Int IEEE/EMBS Conf Neural Eng NER. 2013:593–596.
60. Gandy A, Hahn G. MMCTest-A safe algorithm for implementing multiple monte carlo tests. Scand J Stat. 2014; 41:1083–1101.
61. Harris KD, Henze Da, Csicsvari J, Hirase H, Buzsáki G. Accuracy of tetrode spike separation as determined by simultaneous intracellular and extracellular measurements. J Neurophysiol. 2000; 84:401–414. [PubMed: 10899214]
62. Paxinos, G., Franklin, KBJ. The Mouse Brain in Stereotaxic Coordinates. Academic Press; 2001.

Europe PMC Funders Author Manuscripts

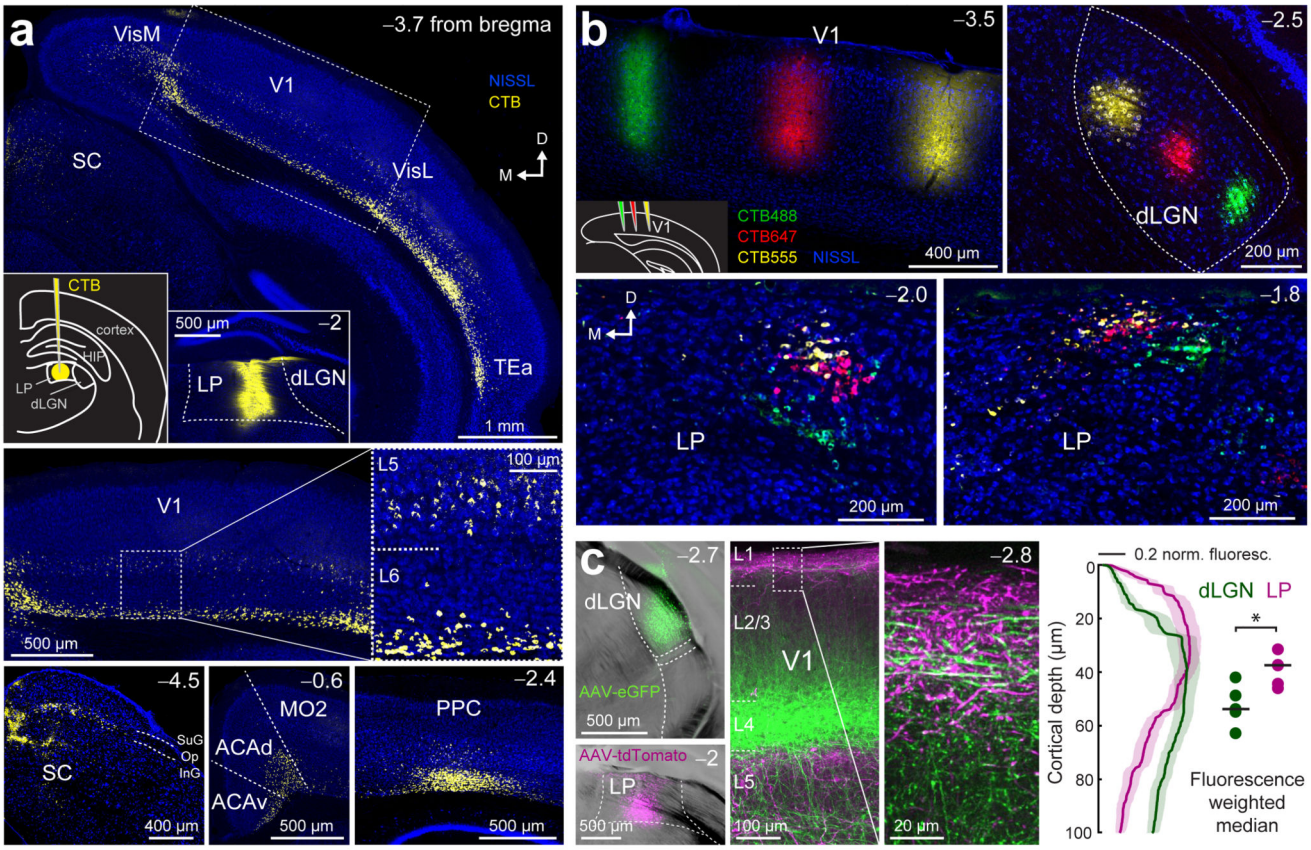

Figure 1. Connectivity of the lateral posterior nucleus (LP)

(**a**) Projections to LP. Retrograde tracer injection into LP (CTB; insets in top panel: left, schematic of the injection; right, injection site) and areas with substantial numbers of retrogradely labelled cell bodies. Top: V1, primary visual cortex; Hip, hippocampus; SC, superior colliculus; TEa, temporal association area; VisM, medial visual areas; VisL, lateral visual areas; Bottom: ACAd, dorsal anterior cingulate cortex; ACAv, ventral anterior cingulate cortex; MO2, secondary motor area; PPC, posterior parietal cortex; SC: superior colliculus, SuG, superficial gray layer; Op, optic layer; InG, intermediate gray layer. Arrows indicate the orientation of the coronal sections (similar for all images in this figure; M: medial; D: dorsal). (**b**) Organization of thalamic neurons projecting to V1 in coronal slices. Top, left panel: three retrograde tracer injections in V1 (see inset in bottom left corner; CTB488, CTB647 and CTB555) at different retinotopic locations. Retrogradely labelled neurons in dLGN (top, right panel) and in LP at two positions along the anterior-posterior axis (bottom panels). (**c**) Projections from LP and dLGN. Double injection of AAV2.1-Ef1a-eGFP into dLGN and AAV2.1-Ef1a-tdTomato into LP (left panels) and pattern of dLGN (green) and LP (magenta) axons in V1 (middle panels with an enlarged inset of layer 1). Right panel: normalized fluorescence intensity of LP (magenta) and dLGN axons (green) at different cortical depths in layer 1. Shaded areas denote s.e.m. Dots: weighted median of maximum fluorescence for individual brain slices. Black lines show the median, P = 0.03, Wilcoxon rank-sum test, n = 5 slices, 2 mice. Observations in **a** and **b** were reproduced in 11 and 3 mice, respectively.

Europe PMC Funders Author Manuscripts

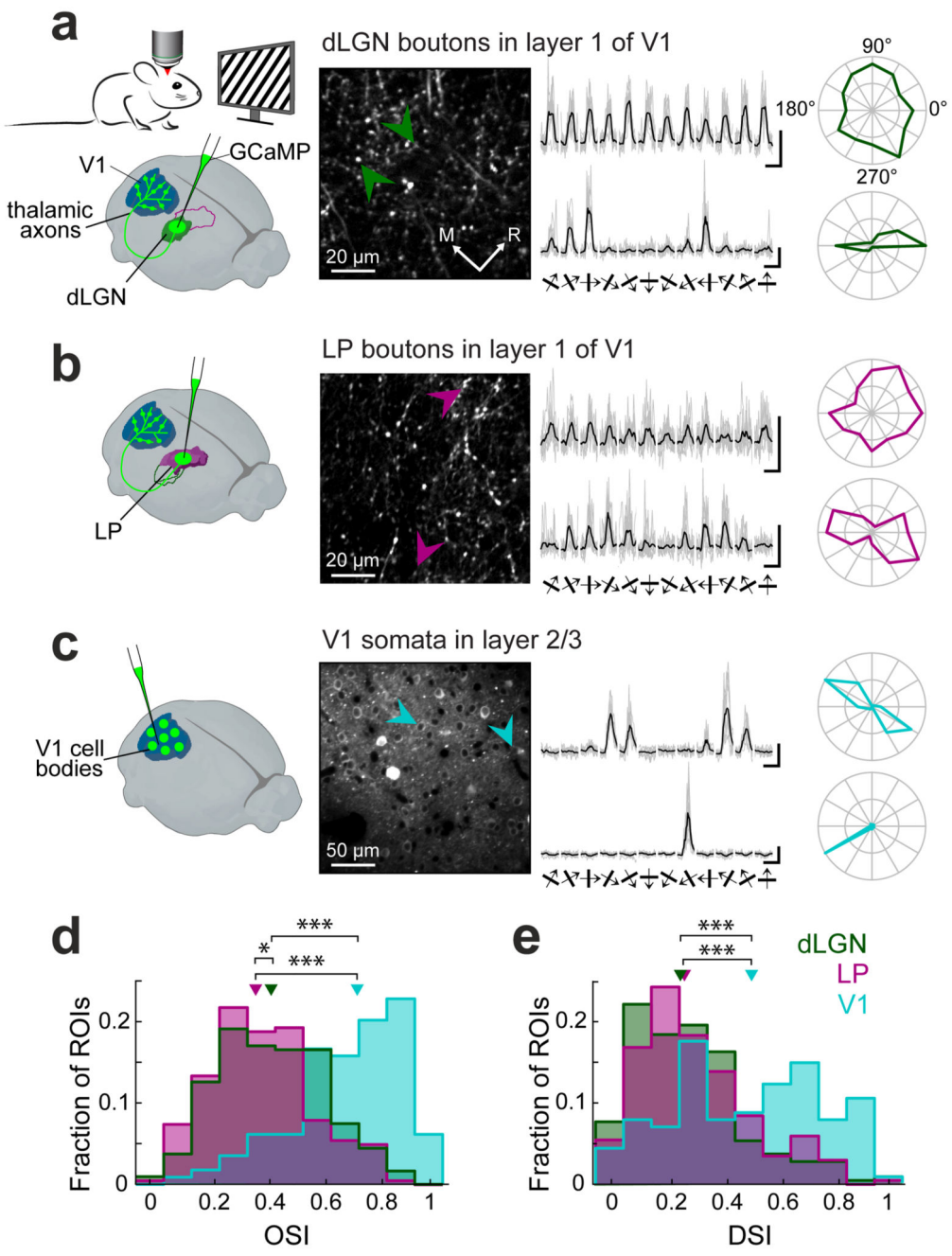

Figure 2. Orientation and direction selectivity of thalamic input to V1.

(**a**) Left, experimental schematic. Imaging responses of thalamo-cortical projections in V1 to drifting square-wave gratings using two-photon microscopy in anaesthetized mice expressing the calcium indicator GCaMP6 in dLGN. Middle, two-photon image of dLGN axons and putative axonal boutons in L1 of V1. Right, example fluorescence traces in response to 12 randomly interleaved grating directions (grey: eight individual repetitions re-ordered according to grating direction, black: average) and polar plots from two dLGN boutons (indicated by arrows; top bouton, OSI = 0.21, DSI = 0.13; bottom bouton: 0.91,

0.2). (**b**) Example responses of thalamo-cortical axonal boutons in L1 of V1 after GCaMP6 expression in the LP. Same layout as in **a**. (top bouton, OSI = 0.29, DSI = 0.38; bottom bouton: 0.81, 0.09) (**c**) Example responses of V1 layer 2/3 neurons. Same layout as in **a**. (top neuron, OSI = 0.95, DSI = 0.09; bottom neuron: 0.93, 0.91). (**d,e**) Distribution of orientation selectivity indices (OSIs, **d**) and direction selectivity indices (DSIs, **e**) of visually-responsive dLGN boutons, LP boutons and V1 cell bodies. Triangles indicate medians. *, $p < 0.05$; ***, $p < 10^{-8}$, Wilcoxon rank-sum test. dLGN: n = 429 boutons, 6 mice, LP: n = 202 boutons, 6 mice, V1: n = 114 cells, 4 mice. All scale bars, 2 ΔF/F, 2 s.

Europe PMC Funders Author Manuscripts

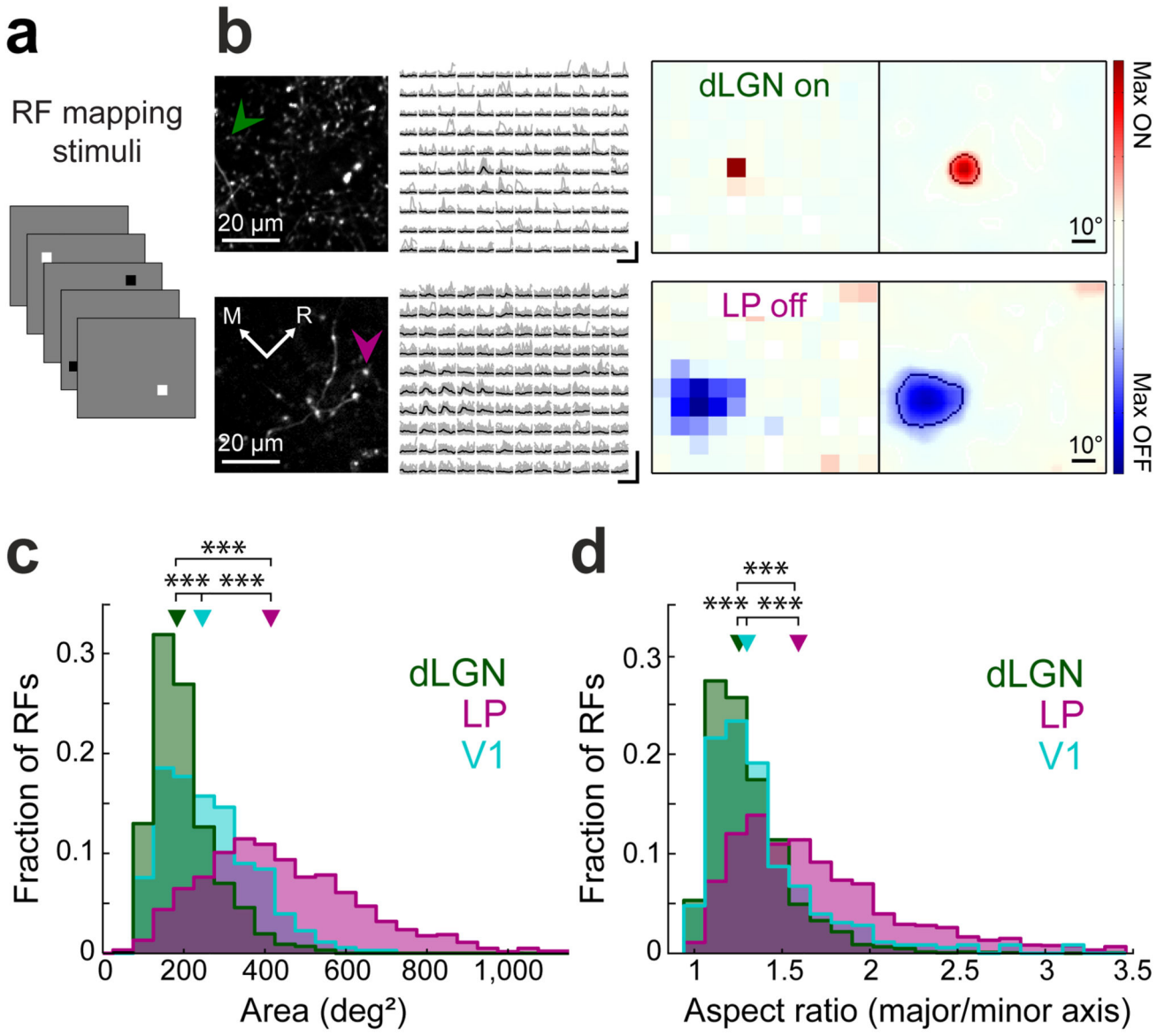

Figure 3. Spatial receptive field properties of thalamic input to V1.

(**a**) Schematic of receptive field mapping stimuli: black and white squares (8 deg x 8 deg) on a gray background. (**b**) Responses of an ON-selective dLGN bouton to white squares (top) and an OFF-selective LP bouton to black squares (bottom) at different positions. Left, two-photon image of dLGN (top) and LP (bottom) projections in L1 of V1. Middle left, example fluorescence traces of a single bouton (indicated by arrows; individual traces in gray, averages in black) ordered according to stimulus position. Scale bars, 400% ΔF/F, 2 s. Middle right, receptive fields of the boutons. Far right, smoothed receptive fields. Line indicates receptive field outline (see Methods). (**c,d**) Distributions of spatial receptive field size (**c**), and the ratio of major to minor axis length of receptive fields (**d**) of dLGN and LP boutons and V1 layer 2/3 cell bodies. Triangles indicate medians. ***, $P < 10^{-10}$, Wilcoxon

rank-sum test. dLGN: n = 2317 receptive fields, 7 mice, LP: 1825 receptive fields, 13 mice, V1: 356 receptive fields, 4 mice.

Europe PMC Funders Author Manuscripts

Europe PMC Funders Author Manuscripts

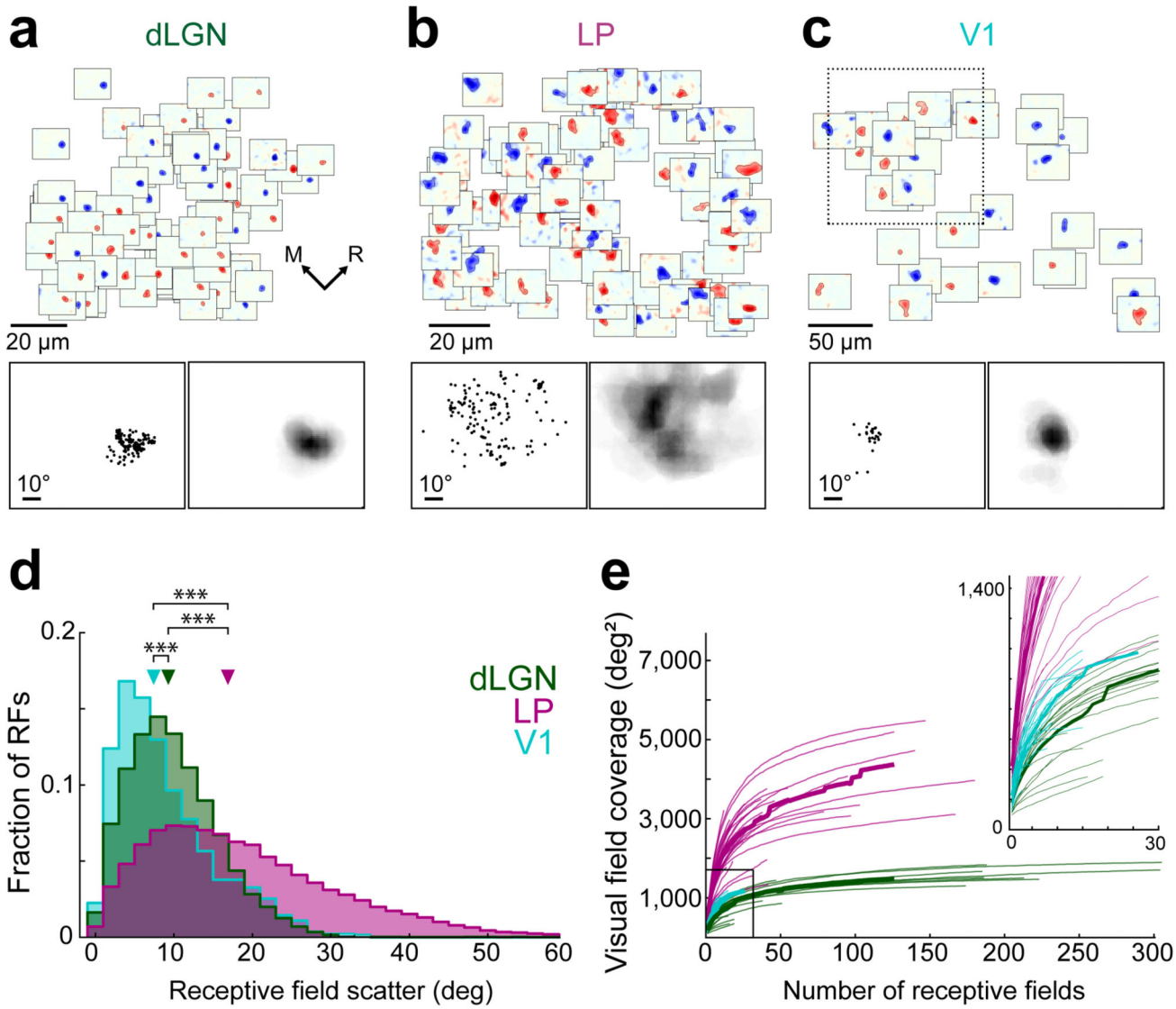

Figure 4. Scatter and visual field coverage of thalamic spatial receptive fields.

(**a**) Example population of all dLGN receptive fields from one 120 µm by 120 µm region in L1 of V1. Top, receptive field subdomains of individual boutons plotted at the boutons' cortical x-y position within the imaged region. Bottom left, positions of subdomain centroids in visual space from the dLGN receptive fields above. Bottom right, sum of all dLGN receptive fields above, illustrating their visual field coverage. (**b**) All LP receptive field subdomains from an example region. Same layout as **a**. (**c**) Population of V1 layer 2/3 neuron receptive field subdomains from an example 250 µm by 250 µm region. Same layout as **a** except that the bottom panels refer to a 120 µm by 120 µm subset of the imaged region above (indicated by dashed-line square). (**d**) Distribution of receptive field scatter, determined by the distances between the centroids of pairs of receptive fields. For neurons or boutons with both ON and OFF subdomains, these were included separately (see Methods). dLGN: n = 273353, LP: n = 87804, V1: n = 1380 pairs of receptive fields. Triangles indicate

medians. ***, $p < 10^{-10}$, Wilcoxon rank-sum test. (**e**) Cumulative area covered by the population receptive field as a function of the number of individual receptive fields. Thin lines indicate individual imaged regions, thick lines indicate medians. dLGN: n = 20 regions, 7 mice, LP: n = 33 regions, 13 mice, V1: n = 8 regions (subdivided into 32), 4 mice.

Europe PMC Funders Author Manuscripts

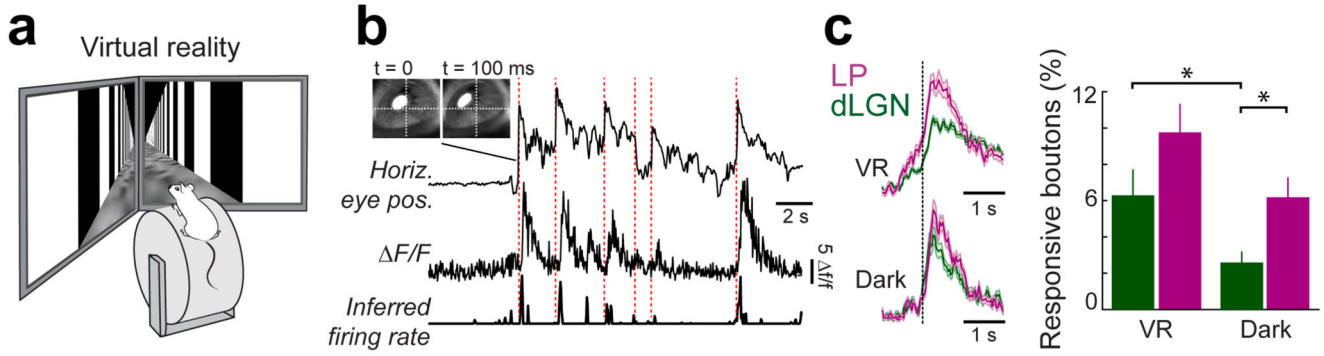

Figure 5. Responses of LP and dLGN boutons to eye movements.

(**a**) Schematic of the virtual reality setup. (**b**) Calcium trace and inferred firing rate of an example bouton aligned to horizontal pupil position of the contralateral eye. Top left: images of the eye taken before and after a saccade. Red dashed lines indicate occurrences of saccades. Pupil position and inferred firing rate in arbitrary units. (**c**) Left: average traces of inferred firing rate (a.u.) of LP and dLGN boutons showing significantly increased activity in response to a saccade, aligned to saccade onset (dashed line) in the virtual environment (VR) and in the dark. Right: mean fraction of LP and dLGN boutons significantly modulated by saccades. Error bars are s.e.m. *, $p < 0.05$, Wilcoxon rank-sum test. VR dLGN, n = 21 sessions ; VR LP, n = 31 sessions; Dark dLGN, n = 21 sessions; Dark LP, n = 30 sessions; LP, 10 mice; dLGN: 8 mice.

Europe PMC Funders Author Manuscripts

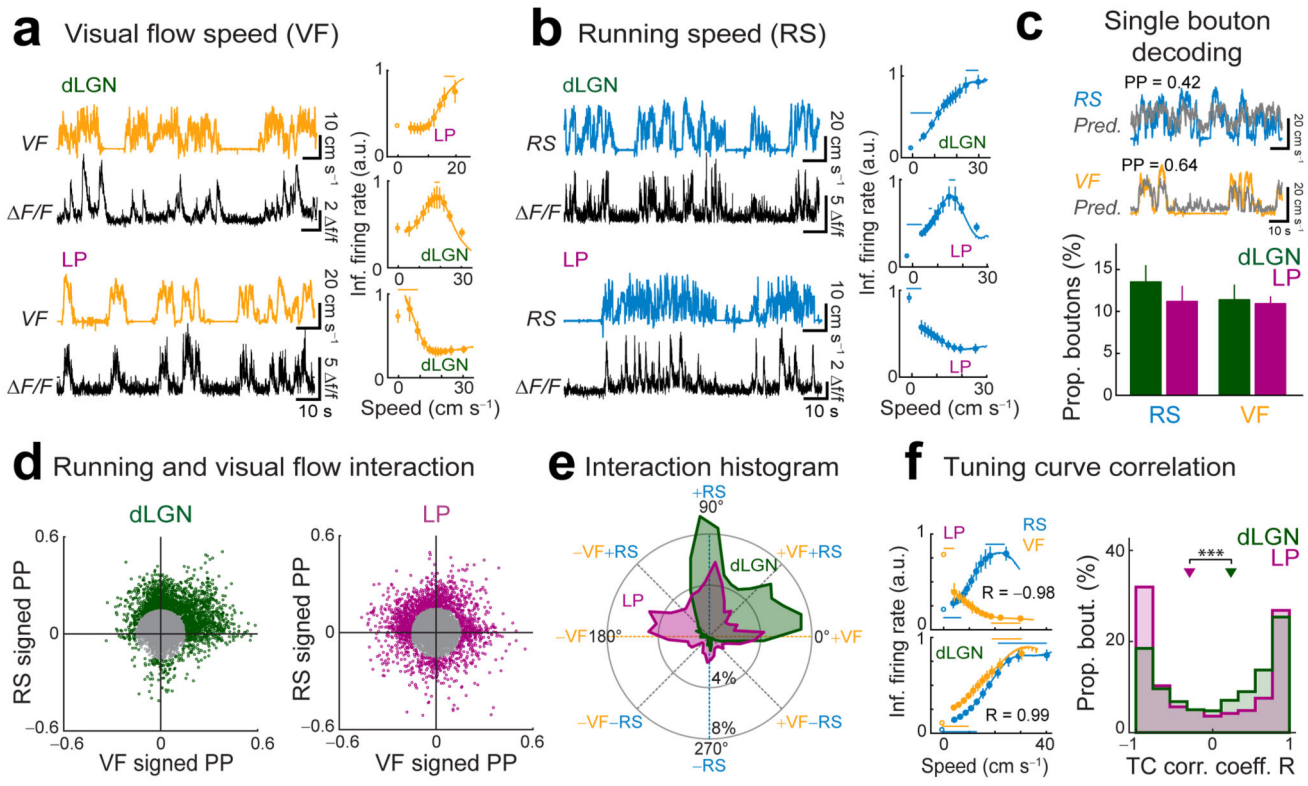

Figure 6. LP and dLGN carry distinct visual, motor and visuo-motor signals.

(**a,b**) Left: calcium traces of two example boutons aligned to visual flow speed (VF) of the virtual corridor (**a**, yellow) or the running speed (RS) of the animal (**b**, blue) in the open-loop condition of the virtual reality (virtual visual flow speed uncoupled from running speed). Right, virtual visual flow speed (**a**) and running speed (**b**) tuning curves for example boutons. Lines above tuning curves indicate significant bins (see Methods). Error bars are s.e.m. (**c**) Top: example traces of RS and VF, over-plotted with model predictions for these traces (gray traces) from a random forest decoder trained with inferred spikes from single example boutons (see Methods). PP: prediction power between observed variable and single-bouton prediction over the whole recording. Bottom: proportions of dLGN and LP boutons conveying significant information (PP > 0.16) about RS or VF. (**d**) Relationship between the 'signed' prediction power (PP) for RS and for VF for all boutons. A sign was assigned to each PP according to the sign of the linear correlation coefficient between activity and RS or VF for each bouton (see Methods). Only boutons with |PP| > 0.16 from the origin (colored points in scatter plots) were included in the analysis in **e** and **f**. (**e**) Circular histogram showing the distribution of LP and dLGN boutons with different interaction angles θ between the 'signed' PP for RS and VF (see manuscript text and Methods). (**f**) Left: tuning curves for RS and VF for two example boutons. Top left: anticorrelated tuning curves typical of boutons with θ ~135° (R, Pearson's correlation coefficient). Bottom left: correlated tuning curves typical of boutons with θ ~45°. Right: distributions of correlation coefficients R between RS and VF tuning curves (TCs) of individual boutons. ***, $P < 10^{-7}$, Wilcoxon rank-sum test. dLGN: n = 2159 boutons, 8 mice, LP: n = 1617 boutons, 10 mice.

Europe PMC Funders Author Manuscripts

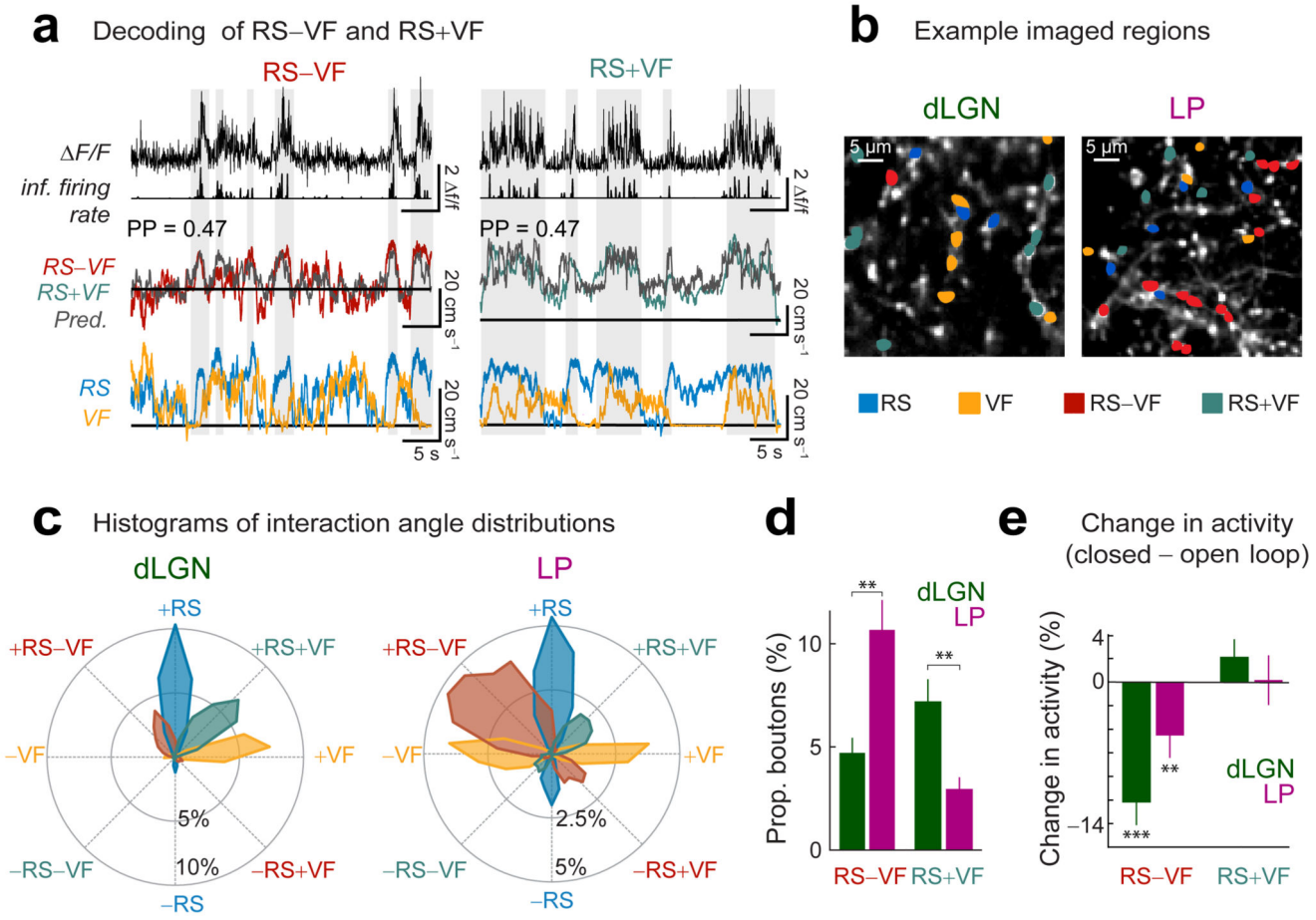

Figure 7. Visuo-motor discrepancy signals are enriched in LP.

(**a**) Calcium traces and inferred firing rate (top) of two example boutons aligned to the difference between running speed and visual flow speed (RS–VF, left) or the equal sum of RS and VF (RS+VF, right), over-plotted with model predictions for these traces (gray) obtained with a random forest decoder trained on inferred spike rates from the example boutons above. PP: prediction power. Bottom: aligned running speed and visual flow speed traces. Gray shaded regions reflect periods of elevated RS−VF or RS+VF (horizontal black lines indicate zero). (**b**) Example imaged regions. Boutons with highest PP for RS, VF, RS–VF or RS+VF are indicated by different colors (if PP > 0.16). (**c**) Circular histogram with distributions of interaction angles θ for different groups of LP and dLGN boutons. Similar to Fig.6e, but boutons were grouped according to which variable they predicted best (groups with highest PP for RS, VF, RS+VF or RS−VF are indicated by different colors). (**d**) Proportions of dLGN and LP boutons with highest PP for RS−VF or RS+VF (if PP > 0.16) out of all boutons. Wilcoxon rank-sum test. dLGN: n = 18 regions, 8 mice, LP: n = 31 regions, 10 mice. (**e**) Average change in activity in the closed-loop condition relative to the open-loop condition for boutons most informative about RS–VF or RS+VF in the open-loop condition (thresholded average *ΔF/F*, see Methods; Wilcoxon signed-rank test; dLGN: RS

Europe PMC Funders Author Manuscripts

+VF, 334 boutons, RS–VF, 206 boutons, n = 10 session pairs, 7 mice, LP: RS+VF, 99 boutons, RS–VF, 276 boutons, n = 13 session pairs, 8 mice.). **, P<0.01; ***, P<10^{-10}.

Europe PMC Funders Author Manuscripts